

Probabilistic Point Cloud Modeling via Self-Organizing Gaussian Mixture Models

Kshitij Goel, Nathan Michael, and Wennie Tabib



Fig. 1: The methodology proposed in this work enables multi-modal reconstruction at varying scales. Without modifying parameters, the methodology models depth and grayscale data of small objects (1 m \times 1 m safety cone in the left image) and complex environments (10 m \times 5 m cave in the center image) while also modeling depth and thermal data of (right) large-scale buildings (42 m \times 28 m) [1]. A supplementary video may be found at <https://youtu.be/v0DfhK1lyno>.

Abstract—This letter presents a continuous probabilistic modeling methodology for spatial point cloud data using finite Gaussian Mixture Models (GMMs) where the number of components are adapted based on the scene complexity. Few hierarchical and adaptive methods have been proposed to address the challenge of balancing model fidelity with size. Instead, state-of-the-art mapping approaches require tuning parameters for specific use cases, but do not generalize across diverse environments. To address this gap, we utilize a self-organizing principle from information-theoretic learning to automatically adapt the complexity of the GMM model based on the relevant information in the sensor data. The approach is evaluated against existing point cloud modeling techniques on real-world data with varying degrees of scene complexity.

Index Terms—Mapping, RGB-D Perception, Field Robots

I. INTRODUCTION

DENSE point cloud data are used in physical simulations [2], computer graphics [3], and robotic perception [4]. For robotic perception applications, in particular, three-dimensional (3D) perception algorithms do not operate directly on raw point cloud data; instead, they subsample, discretize, or create an intermediate representation [5]. Gaussian mixture models (GMMs) have been proposed as a generative model to compactly parameterize raw point cloud data [6–8] and enable high-resolution transmission of perceptual information to other robotic systems in communication restricted environments [9, 10]. These models have been leveraged to represent occupancy [8], estimate pose [11], and perform incremental mapping [7, 12], which are fundamental subsystems for higher-level robot autonomy. However, these prior works require model complexity selection before operation and do not adapt based on three-dimensional structure. We address

this gap by proposing a GMM-based point cloud modeling technique which adapts the number of components according to the scene complexity (Fig. 1).

The fundamental challenge is to estimate the number of components required to model the point cloud to obtain sufficient fidelity. McLachlan and Rathnayake [13] provide an overview of approaches to estimate the number of components in a GMM. Among the commonly used criteria are the Akaike’s information criterion (AIC) [14], Bayesian information criterion (BIC) [15], and Model description length (MDL) [16], which strike a balance between the fit over the underlying dataset and model complexity. For example, to use AIC or BIC scores for model selection one must plot the scores over many candidate mixtures with increasing numbers of components to detect an approximate minima, which is prohibitive for online robotics applications with finite computational power and timing constraints. Variational methods have been created to estimate *a posteriori* distributions over the parameters of a GMM; however, these methods also require specifying a prior distribution over model parameters [17, 18].

Contributions. In contrast to these methods, this work proposes a perceptual modeling methodology that reduces the redundancy in a dataset and extracts the *relevant* information via a self-organizing principle called the Principle of Relevant Information (PRI). We call this approach the *Self-Organizing Gaussian Mixture Modeling* (SOGMM) method as it adapts the number of components of a GMM via self-organization. The rest of the paper is structured as follows. Section II reviews related work in point cloud modeling for robotic perception. Section III presents the details of the SOGMM method and Section IV provides evaluation on real-world point cloud data. We conclude this letter and discuss future work in Section V.

*The authors are with The Robotics Institute, Carnegie Mellon University, Pittsburgh, PA 15213 USA (email: {kshitij, nmichael, wtabib}@cmu.edu).

II. RELATED WORK

In this section, we focus on reviewing methods that enable probabilistic modeling of multi-modal point cloud data for high-fidelity reconstruction.

Discrete Methods. Robotics applications commonly leverage probabilistic environment representations consisting of fixed-size volumetric pixels (or voxels in 3D) and represent occupancy as independent, discrete random variables [19]. The discrete probability distribution is updated using the inverse sensor model and Bayes’ rule. The limitation of this representation is it requires specifying parameters such as voxel size and occupancy clamping thresholds, which are dependent on environmental conditions. Although the compute usage for Bayesian updates is low, voxel grids require significant memory to scale in spatially-extensive environments. Multi-modal extensions for 3D voxel grids suffer from the same limitations [20].

To reduce the number of voxels, Magnusson et al. [21] propose the Normal Distributions Transform mapping framework (NDTMap) that utilizes the same volumetric factorization but places a Gaussian distribution in each occupied voxel. The Voxblox method by Oleynikova et al. [22] uses truncated signed distance functions (TSDFs) over regular 3D voxel grids for point cloud modeling as opposed to an occupancy-based formulation. Both of these frameworks model the point cloud with less memory than regular 3D voxel grids, but still require specifying a map resolution in advance.

Hornung et al. [23] present OctoMap to address the limitation regarding pre-specified voxel resolution via the hierarchy of an octree. The limitations are that pre-specifying a minimum leaf size, which determines the maximum size of the map, and occupancy thresholds are still required. Recent advances over OctoMap demonstrate improvements in compression and fidelity [24, 25]; however, the limitations regarding pre-specified parameters are unaddressed.

In contrast to these discrete methods, we present a continuous probabilistic multi-modal modeling methodology that adapts the model complexity according to the scene variation.

Continuous Methods. Continuous non-parametric point cloud modeling methods like Gaussian Process (GP) [26] and Hilbert maps [27] increase representational power at the expense of high computational cost. Closest to our work, Zobeidi et al. [28] develop an incremental metric-semantic GP mapping approach that represents map uncertainty and outperforms deep neural network-based approaches. However, the need for offline training and specification of model hyperparameters precludes the use of this representation for online adaptive compression. Yan et al. [29] present a highly-parallelized adaptive scene representation that utilizes a Dirichlet Process (DP) mixture model as a point cloud model. However, an upper limit on the number of components allowed per processor must be pre-specified, which limits the adaptability of the resulting model.

Neural Implicit Representations (NIRs) have been proposed as continuous implicit models for radiance and occupancy information. Most works in this area build on Neural Radiance Fields (NeRFs) proposed by Mildenhall et al. [30]. While

NeRFs produce high-resolution, realistic models, they suffer from one major limitation due to the fixed architecture of the underlying neural network, which does not allow adaptivity in the representation of the scene.

Generative probabilistic models that use a finite mixture of probability distributions aim to represent the environment through an adaptive and parametric mathematical model, and thus provide a potential solution to the limitation in adaptivity of NeRFs. Recently, Gaussian mixture models (GMMs) have been utilized for adaptive point cloud modeling [6–8, 31, 32]. Eckart et al. [6] use a top-down hierarchy of 3D GMMs to represent 3D point cloud data at different levels of detail. Srivastava and Michael [7] use a bottom-up hierarchy of 4D GMMs to model the surface point clouds and the points along the sensor beams. Navarrete et al. [31] modify the FastGMM framework by Greggio et al. [33] and use it for compressing locally planar point clouds. The FastGMM approach creates a GMM via a deterministic splitting criterion in a coarse-to-fine manner. Dong et al. [32] use a similar idea for adaptive model selection in their GMM mapping approach. The Gaussian components belonging to the same plane are merged using their mean vectors and principal directions to obtain a coarser model. Common to all these works is a requirement to specify the levels of detail; either directly (e.g., number of layers in hierarchy of GMMs) [6] or indirectly (e.g., through convergence, splitting, or merging criteria) [7, 31, 32]. Specifying these parameters *a priori* can be challenging for real-world robotic applications.

In contrast to these methods, the proposed approach does not require processing a hierarchy of GMMs to achieve online adaptation with respect to scene complexity. Instead, we perform model selection for GMMs through information-theoretic learning as described in the next section.

III. APPROACH

Notation. In this section, small letters are used for scalars and univariate random variables (e.g., w, h, x, g), capital letters for multivariate random variables (e.g., X, Y), bolded small letters for vectors (e.g., \mathbf{x}, \mathbf{y}), bolded capital letters for matrices (e.g., \mathbf{X}, \mathbf{Y}), and calligraphic letters for sets (e.g., $\mathcal{I}, \mathcal{X}, \mathcal{Y}$). The probability density of a continuous multivariate random variable X is written as $p_X(\mathbf{x})$, where \mathbf{x} is a value in the sample space of X .

Overview. An overview of the SOGMM system is shown in Fig. 2. We assume that a registered pair of depth, $\mathbf{I}_d \in \mathbb{R}^{h \times w}$, and grayscale, $\mathbf{I}_g \in \mathbb{R}^{h \times w}$, images $\mathcal{I} := \{\mathbf{I}_d, \mathbf{I}_g\}$ of dimension $h \times w$ is provided for point cloud modeling. Note that the grayscale modality can also be thermal data (e.g., the building in Fig. 1) scaled to a range $[0, 1]$. The image frame points may be projected to three dimension using the intrinsic camera matrix and associated with depth to obtain a pointcloud \mathcal{X} with hw points, where each point $\mathbf{x}_i \in \mathcal{X}$ is four-dimensional and consists of 3D coordinates (x, y, z) augmented with a grayscale value g . Like prior works in GMM-based point cloud modeling [4, 6, 35], we assume that the points in \mathcal{X} are independently and identically distributed (i.i.d.) samples from an underlying continuous random variable

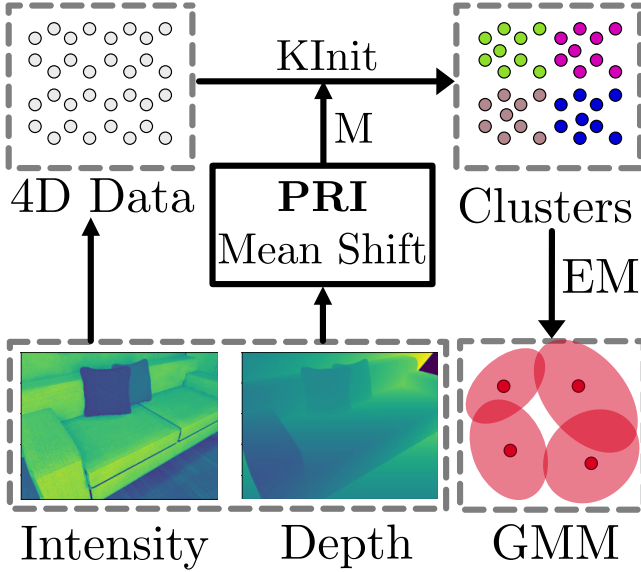


Fig. 2: Overview of the proposed point cloud modeling method. The registered intensity-depth image pair is used by the PRI component to determine the number of modes M . Steps (1a)–(1c) of the K-Means++ algorithm [34] perform a hard-partitioning of the 4D data into M clusters (KInit). Finally, the EM algorithm does a soft-partitioning of the 4D data using the KInit output to create a M -component finite GMM. The proposed system encodes the 4D point cloud data into a finite GMM without requiring the specification of number of mixtures M for every image pair.

X . The goal of the proposed approach is to model the joint probability distribution $p(x, y, z, g)$ as a GMM, $\mathcal{G}(\mathcal{I})$. Thus, the probability density for $\mathcal{G}(\mathcal{I})$ is written as:

$$\mathcal{G}(\mathcal{I}) \equiv p_X(\mathbf{x}) = \sum_{m=1}^M \pi_m \mathcal{N}(\mathbf{x} | \boldsymbol{\mu}_m, \boldsymbol{\Sigma}_m), \quad (1)$$

where, $\pi_m \in \mathbb{R}$, $\boldsymbol{\mu}_m \in \mathbb{R}^4$, and $\boldsymbol{\Sigma}_m \in \mathbb{R}^{4 \times 4}$ are the weight, mean, and covariance associated with the m^{th} multivariate Gaussian distribution component of the mixture. In contrast to existing techniques where the number of mixtures is specified *a priori* [10, 36] or utilize a hierarchy of GMMs to estimate the number of components [6, 35], the contribution of this work is a self-organizing approach that learns the number of mixtures from the underlying sensor data, \mathcal{I} , via information-theoretic techniques. This learned value is used for generative modeling for dataset \mathcal{X} via the Expectation-Maximization (EM) algorithm [37], and utilizes steps (1a)–(1c) of K-Means++ [34] for initialization. The output of EM is the model $\mathcal{G}(\mathcal{I})$ from Eq. (1). Since this model is a joint distribution over the 3D spatial coordinates and the grayscale data, we can use the conditional distribution $p(g | [x \ y \ z]^T)$ to regress the grayscale image from the model for a given spatial point cloud and pinhole camera model [35, 38]. The remainder of this section describes how to estimate the number of mixture components M .

Principle of Relevant Information. The Principle of Relevant Information (PRI) [39] is an approach that extracts the relevant statistics from the dataset to learn a compressed representation of size M , equal to the number of locally-dense regions in the environment. The intuition behind PRI

is to extract these relevant statistics by simultaneously minimizing the redundancy and distortion between the original and compressed datasets. Formally, let us consider a dataset, \mathcal{Y} , in which the points are assumed to be D -dimensional i.i.d. samples from a continuous multivariate random variable Y with the associated probability density function $p_Y(\mathbf{y})$. To create a compressed dataset \mathcal{Y}_r , with random variable Y_r and density $p_{Y_r}(\mathbf{y})$, the PRI is an information-theoretic optimization problem with the objective function:

$$J(Y_r) = \min_{Y_r} H_2(Y_r) + D_{CS}(Y_r, Y), \quad (2)$$

where, $H_2(Y_r)$ is the Renyi's quadratic entropy (RQE) of dataset \mathcal{Y}_r calculated using the density $p_{Y_r}(\mathbf{y})$ and $D_{CS}(Y_r, Y)$ is the Cauchy-Schwarz divergence (CSD) between datasets \mathcal{Y}_r and \mathcal{Y} calculated using the densities $p_{Y_r}(\mathbf{y})$ and $p_Y(\mathbf{y})$. Minimizing RQE ensures less redundancy in the compressed dataset and minimizing CSD reduces the error induced due to compression. Principe [39] proves that when RQE and CSD have an equal contribution to the objective function in Eq. (2), the compressed dataset \mathcal{Y}_r contains the modes of the original dataset \mathcal{Y} .

Gaussian Mean Shift. Rao et al. [40] show that the Gaussian Mean Shift (GMS) algorithm, as proposed by Cheng [41], is an iterative scheme for an approximate solution to the optimization problem in Eq. (2). The GMS algorithm uses a nonparametric estimate of the density $p_Y(\mathbf{y})$,

$$p_Y(\mathbf{y}) = \frac{1}{|\mathcal{Y}|} \sum_{i=1}^{|\mathcal{Y}|} K_{\mathbf{H}}(\mathbf{y} - \mathbf{y}_i), \quad (3)$$

where, \mathbf{H} is a symmetric positive definite $D \times D$ matrix and $K_{\mathbf{H}}(\mathbf{y} - \mathbf{y}_i)$ is a multivariate symmetric Gaussian kernel. This matrix is usually chosen proportional to the identity matrix $\mathbf{H} = \sigma^2 \mathbf{I}_{D \times D}$, where σ is called the *bandwidth* parameter [42]. Under this assumption the kernel $K_{\mathbf{H}}(\mathbf{y} - \mathbf{y}_i)$ simplifies to:

$$K_{\mathbf{H}}(\mathbf{y} - \mathbf{y}_i) = \frac{1}{(2\pi)^{D/2} \sigma} \exp\left(-\frac{1}{2\sigma^2} \|\mathbf{y} - \mathbf{y}_i\|^2\right). \quad (4)$$

The compressed dataset \mathcal{Y}_r containing the modes of the dataset is constructed through successive iterations using the update rule:

$$\mathbf{y}_{r,i}^t \leftarrow \frac{\sum_{j=1}^{|\mathcal{Y}|} K_{\mathbf{H}}(\mathbf{y}_{r,i}^{t-1} - \mathbf{y}_j^0) \mathbf{y}_j^0}{\sum_{j=1}^{|\mathcal{Y}|} K_{\mathbf{H}}(\mathbf{y}_{r,i}^{t-1} - \mathbf{y}_j^0)}, \quad (5)$$

where, the indices i and j iterate over each point in \mathcal{Y} and the index $t \in \{0, \dots, T-1\}$ is used to indicate a GMS iteration. At $t = 0$, the compressed dataset is initialized with the original dataset $\mathcal{Y}_r^0 = \mathcal{Y}^0$. The convergence criteria for GMS is based on the relative change in the points between successive iterations or the maximum number of iterations T [43]. At the final iteration, the dataset contains many overlapping points (indicating modes) and is filtered based on Euclidean distances to obtain the final output \mathcal{Y}_r .

Mean Shift on Image Pair. For the SOGMM system, we set the value of M for a given image pair \mathcal{I} to be the number of unique points in the reduced dataset, i.e., $M = |\mathcal{Y}_r|$. In contrast to applying the mean shift algorithm in \mathbb{R}^4 using the

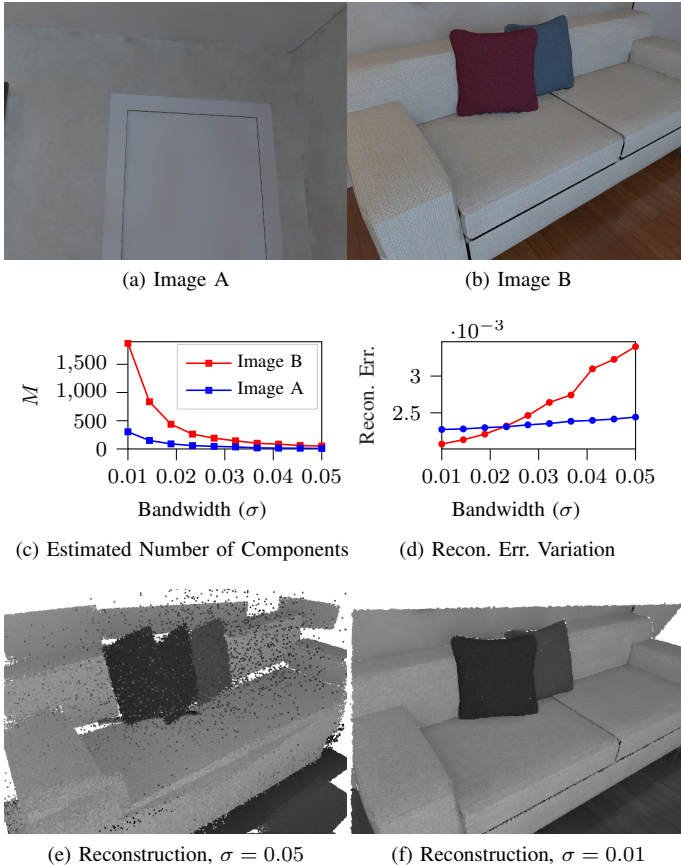


Fig. 3: A study on how the PRI (Eq. (1)) component in the SOGMM system (Fig. 2) adapts the model size according to the scene complexity. A simple scene consisting of (a) homogeneous, white walls requires fewer components than a (b) complex scene consisting of discrete, structured objects. (c) plots the number of components required to represent each of the two scenes for a given bandwidth parameter, σ . (d) plots the mean reconstruction error variation with σ . (e) and (f) show the reconstruction result for the extrema bandwidths in (d). Note how the SOGMM formulation selects more components to represent the complex scene for a given bandwidth value. Further, the reconstruction error varies monotonically with σ .

point cloud \mathcal{X} , we create the dataset \mathcal{Y} from Eq. (2) in \mathbb{R}^2 space using depth and grayscale values from the image pair \mathcal{I} . Each point \mathbf{y} in the dataset is a tuple (d_i, g_i) , such that $d_i \in \mathbf{I}_d$, $g_i \in \mathbf{I}_g$, and i is an index for a pixel coordinate in the images. Thus, the size of the dataset \mathcal{Y} is hw (equal to that of \mathcal{X}) and $D = 2$.

The time complexity of the GMS algorithm increases quadratically with the number of points, linearly with the number of iterations, and linearly with the dimension of the data, $\mathcal{O}(TD|\mathcal{Y}|^2)$ [44]. The number of iterations for convergence T depends on the bandwidth value σ . In general, lower values of σ require larger values of T . For faster convergence, Carreira-Perpiñán [43] propose a modification to the update rule in Eq. (5) called the Gaussian Blurring Mean Shift (GBMS) algorithm and an early stopping criteria to obtain similar results. Instead of using the iterate \mathbf{y}_j^0 for every iteration in Eq. (5), GBMS uses the result from the previous

iteration \mathbf{y}_j^{t-1} :

$$\mathbf{y}_{r,i}^t \leftarrow \frac{\sum_{j=1}^{|\mathcal{Y}|} K_{\mathbf{H}}(\mathbf{y}_{r,i}^{t-1} - \mathbf{y}_j^{t-1}) \mathbf{y}_j^{t-1}}{\sum_{j=1}^{|\mathcal{Y}|} K_{\mathbf{H}}(\mathbf{y}_{r,i}^{t-1} - \mathbf{y}_j^{t-1})}. \quad (6)$$

Further, Comaniciu and Meer [42] show that utilizing a flat kernel as opposed to a Gaussian kernel also produces reasonable accuracy in applications like image segmentation while saving substantial computation due to the finite support of the flat kernel. As opposed to the Gaussian kernel in Eq. (4), the flat kernel is given by:

$$K_{\mathbf{H}}(\mathbf{y} - \mathbf{y}_i) = \begin{cases} 1 & \text{if } \|\mathbf{y} - \mathbf{y}_i\| \leq \sigma \\ 0 & \text{if } \|\mathbf{y} - \mathbf{y}_i\| > \sigma \end{cases}. \quad (7)$$

In this work, we utilize both of these approximations to make PRI tractable for dense image pair data.

Figure 3 illustrates a result of applying the method on image pairs corresponding to a scene with low variation in depth and intensity (Fig. 3a) and a scene with high variation in depth and intensity (Fig. 3b). For increasing values of the bandwidth parameter σ used by the kernel in Eq. (5), we observe a monotonic decrease in the estimated number of components (Fig. 3c) and increase in the mean reconstruction error (Figs. 3d to 3f). Further, for the scene in Fig. 3b, the estimated value of M is higher for all bandwidth values compared to the scene in Fig. 3a. This behavior is desired for the SOGMM system as the value of M in the model given by Eq. (1) must adapt automatically according to the scene complexity. Thus, using this system, adaptive complexity in GMM-based point cloud modeling can be achieved by only specifying the bandwidth parameter σ . The choice of bandwidth parameter can be based on the amount of computation available and the level of fidelity in the GMM model required by the application.

IV. EVALUATION

In this section, the performance of the SOGMM method is evaluated on real-world point cloud data provided by Zhou and Koltun [45]: *stonewall* (Fig. 4a), *copyroom* (Fig. 4b), and *lounge* (Fig. 4c). Because the proposed methodology addresses efficient and compact perceptual modeling within the robotics context, it is compared against four open source mapping baselines: (1) OctoMap (OM) [23], (2) NDTMap (NDT) [21], (3) GPOctoMap (GPOM) [46], and (4) GMM with fixed number of components (FC) [4]. The voxel resolutions for the first two approaches are set to 0.02 m and 0.05 m, which have been demonstrated to be adequate for scene representation [29]. A resolution of 0.02 m is used for GPOctoMap. The default maximum variance parameter is lowered to 0.001 from the default 0.02 for better reconstruction quality. For this section only, the following shorthand is introduced: an OM with 0.05 m and 0.02 m leaf sizes will be referred to as OM-0.05 and OM-0.02, respectively; an NDTMap with voxel resolutions of 0.05 m and 0.02 m will be referred to as NDT-0.05 and NDT-0.02, respectively; a GPOM with 0.02 m will be referred to as GPOM-0.02; the GMM approach with 75, 500, and 2000 components will

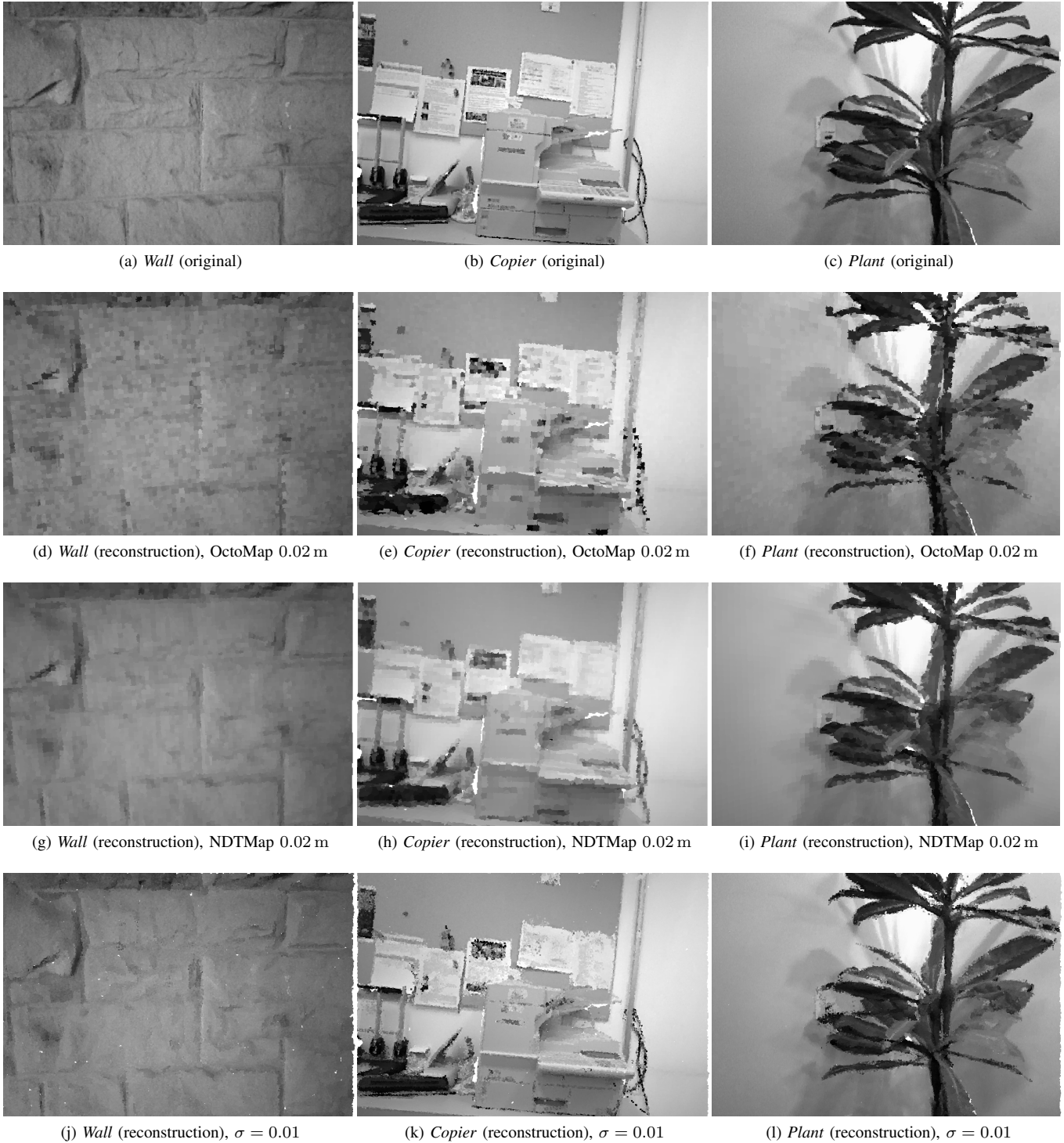


Fig. 4: Resampled output from SOGMMs created for three point clouds with different levels of complexity. The point clouds are taken from real-world datasets [45]. The OctoMap method results in a pixelated output. NDTMap allows a smoother output at a cost of high memory usage. The SOGMM method adapts the complexity of the mixture model without changing parameters across different scenes ($\sigma = 0.01$ for all the cases). A supplementary video may be found at <https://youtu.be/v0DfhK1lyno>.

be referred to as FC-75, FC-500, and FC-2000, respectively; and the SOGMM approach with bandwidths 0.01, 0.02, and 0.03 will be referred to as SOGMM-0.01, SOGMM-0.02, and SOGMM-0.03, respectively.

Reconstruction from Environment Models. For OctoMap, the reconstruction at the minimum leaf size is utilized after modeling occupied space using the `ColorOcTree` class¹. GPOctoMap does not natively support color in the octree nodes², so this support was added for our analysis³. For NDTMap, the reconstruction is obtained by modifying the `NDTCell` class to store the average grayscale value for the points associated with the cell⁴. In both cases, intensity is queried at a 3D coordinate. For the FC and SOGMM approaches, the 3D reconstruction is obtained by densely sampling the joint distribution $p_X(\mathbf{x})$. The grayscale reconstruction is obtained by regressing the expected value from the conditional distribution $p_{g|\mathbf{x}}(g|\mathbf{x})$. This conditional distribution is obtained as follows. First, for each component m in the model given by Eq. (1), the mean and covariance can be written as:

$$\boldsymbol{\mu}_m = \begin{bmatrix} \boldsymbol{\mu}_{m,\mathbf{x}} \\ \boldsymbol{\mu}_{m,g} \end{bmatrix} \quad \boldsymbol{\Sigma}_m = \begin{bmatrix} \boldsymbol{\Sigma}_{m,\mathbf{x}\mathbf{x}} & \boldsymbol{\Sigma}_{m,\mathbf{x}g} \\ \boldsymbol{\Sigma}_{m,g\mathbf{x}} & \boldsymbol{\Sigma}_{m,gg} \end{bmatrix}.$$

The conditional distribution $p_{g|\mathbf{x}}(g|\mathbf{x})$ can be expressed using these quantities as [38]:

$$p_{g|\mathbf{x}}(g|\mathbf{x}) = \sum_{m=1}^M w_m(\mathbf{x}) \mathcal{N}(g | \lambda_m(\mathbf{x}), \nu_m^2), \quad (8)$$

where

$$w_m(\mathbf{x}) = \frac{\pi_m \mathcal{N}(\mathbf{x} | \boldsymbol{\mu}_{m,\mathbf{x}}, \boldsymbol{\Sigma}_{m,\mathbf{x}\mathbf{x}})}{\sum_{m'=1}^M \pi_{m'} \mathcal{N}(\mathbf{x} | \boldsymbol{\mu}_{m',\mathbf{x}}, \boldsymbol{\Sigma}_{m',\mathbf{x}\mathbf{x}})},$$

$$\lambda_m(\mathbf{x}) = \boldsymbol{\mu}_{m,g} + \boldsymbol{\Sigma}_{m,g\mathbf{x}} \boldsymbol{\Sigma}_{m,\mathbf{x}\mathbf{x}}^{-1} (\mathbf{x} - \boldsymbol{\mu}_{m,\mathbf{x}}),$$

and

$$\nu_m^2 = \boldsymbol{\Sigma}_{m,gg} - \boldsymbol{\Sigma}_{m,g\mathbf{x}} \boldsymbol{\Sigma}_{m,\mathbf{x}\mathbf{x}}^{-1} \boldsymbol{\Sigma}_{m,\mathbf{x}g}.$$

Finally, the expected value for Eq. (8) is:

$$\lambda(\mathbf{x}) = \sum_{m=1}^M w_m(\mathbf{x}) \lambda_m(\mathbf{x}). \quad (9)$$

Qualitative Evaluation. Figure 4 provides a qualitative evaluation of the OctoMap, NDTMap, and SOGMM. Figures 4a to 4c provide images of low, medium, and high complexity scenes, respectively. The OctoMap edge effects at the voxel boundaries prevents smooth color representation (see Figs. 4d to 4f). The NDTMap representation can be sampled using the Gaussian components in each voxel, which results in a qualitatively better reconstruction (Figs. 4g to 4i) compared to OctoMap at a cost of high memory

footprint. The SOGMM representation is sampled to generate reconstructions shown in Figs. 4j to 4l, respectively. While the bandwidth parameter remains constant across scenes, the estimated number of components increases with the scene complexity. It is evident that the fine details and intensity are preserved in the edges around the stones (Fig. 4j), thin wires (Fig. 4k), and in the leaves and shadows (Fig. 4l). The SOGMM framework preserves fine details by learning the appropriate model complexity from the underlying sensor data without parameter tuning from the user.

Quantitative Evaluation. The Peak Signal-To-Noise Ratio (PSNR), Mean Reconstruction Error (MRE), and (3) Memory Usage are used for quantitative evaluation. The PSNR quantifies how accurately intensity is reconstructed from the model by comparing against the original intensity image. The MRE is computed for the spatial part of the reconstructed point cloud (i.e., $[x, y, z]^T$) and is given by the average distance between the reconstructed point cloud and the ground truth point cloud. The memory usage quantifies the memory required to store the model in megabytes (MB). For OctoMap, this value is the size of the `.ot` file that retains the occupancy and grayscale information. Note that unlike OctoMap, the GPOctoMap implementation does not enable serialized storage of the octree. Therefore, the GPOctoMap approach is compared on the PSNR and MRE metrics, only. Each cell of the NDTMap stores a Gaussian component and intensity, so the memory usage (assuming floating point values and M cells) is calculated as $4 \cdot M \cdot (1 + 3 + 6)$ bytes. The FC and SOGMM are composed of M 4D Gaussian components, so the memory usage is calculated as $4 \cdot M \cdot (1 + 10 + 4)$ bytes.

Figure 5 provides a comparison of our approach against the OM, NDT, and FC baselines for the *Wall*, *Copier*, and *Plant* scenes shown in Fig. 4. The OM baseline exhibits lower PSNR values (Fig. 5a) and highest reconstruction error (Fig. 5b) compared to other approaches. NDT-0.05 and NDT-0.02 outperform OM-0.05 and OM-0.02 in terms of PSNR and reconstruction error but consume larger amounts of memory (Fig. 5c).

While FC-75, FC-500, and FC-2000 consume less memory compared to NDT-0.02, the approach is not adaptive. As a result, homogenous scenes will be represented with more fidelity than required and complex scenes will have insufficient fidelity, which is undesirable. In contrast, the SOGMM cases adapt to use fewer components for *Wall* and progressively higher numbers of components for *Copier* and *Plant*. Consequently, we observe similar PSNR and reconstruction error scores for SOGMM-0.01 and FC-2000; however, the former case adapts to the scene and consumes less memory for the *Wall* and *Copier* cases. Table I provides raw evaluation data to directly compare SOGMM-0.01 against GPOM-0.02 and the best performing variants of OctoMap, NDT, and FC. GPOM-0.02 enables gains in PSNR and MRE compared to OM-0.02 but the accuracy is lower compared to the NDT, FC, and SOGMM approaches. SOGMM-0.01 produces a model with accuracy in line with NDT-0.02, while consuming significantly less memory. FC-2000 allows higher PSNR scores but overestimates the number of components for scenes with relatively less intensity-depth variation. SOGMM-0.01 on the other hand

¹<https://github.com/OctoMap/octomap/blob/devel/octomap/include/octomap/ColorOcTree.h>

²https://github.com/RobustFieldAutonomyLab/la3dm/blob/master/include/gpocmap/gpocmap_node.h

³https://github.com/kshitijgoel007/la3dm/blob/feature/colcon/include/gpocmap/gpocmap_node.h

⁴https://github.com/OrebroUniversity/perception_oru/blob/port-kinetic/ndt_map/include/ndt_map/ndt_cell.h

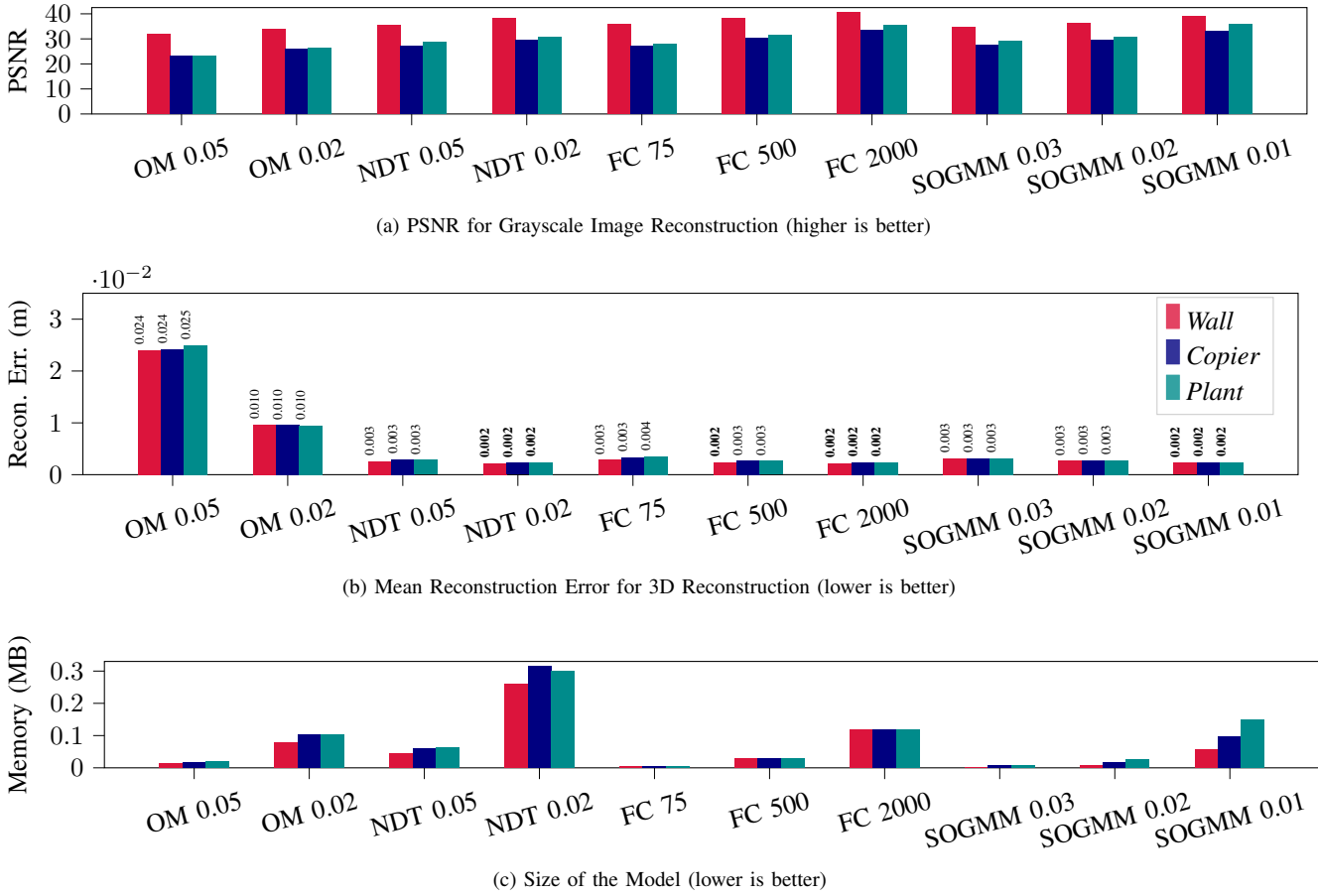


Fig. 5: Quantitative evaluation of the SOGMM method for the scenes shown in Fig. 4. The SOGMM approach enables high accuracy (a) grayscale and (b) 3D reconstructions while allowing (c) adaptation in the size of the model without changing the bandwidth parameter across scenes.

Dataset	OM-0.02			GPOM-0.02			NDT-0.02			FC-2000				SOGMM-0.01								
	PSNR (dB)	MRE (m)	Mem. (MB)	PSNR (dB)	MRE (m)	Mem. (MB)	PSNR (dB)	MRE (m)	Mem. (MB)	PSNR (dB)	MRE (m)	Mem. (MB)	# Voxels	PSNR (dB)	MRE (m)	Mem. (MB)	# Comp.	PSNR (dB)	MRE (m)	Mem. (MB)	# Comp.	
Wall	33.9	0.010	0.078	34.0	0.009		38.0	0.002	0.26	6482	40.5	0.002	0.12	2000	39.1	0.002	0.06	933				
Copier	25.8	0.010	0.10	25.8	0.009		30.0	0.002	0.31	7856	33.4	0.002	0.12	2000	33.0	0.002	0.10	1599				
Plant	26.3	0.010	0.10	26.4	0.009		30.8	0.002	0.30	7470	35.5	0.002	0.12	2000	36.0	0.002	0.15	2464				

TABLE I: Raw data for the quantitative comparison of the OM-0.02, NDT-0.02, FC-2000 and SOGMM-0.01 cases. The SOGMM method achieves a balance between the model fidelity and size for diverse scenes without changing the single tunable parameter σ . The memory is not computed for GPOM-0.02 because the implementation does not provide functions to serialize the perceptual model.

provides a variation in the number of components used without changing any parameters across the three scenes.

SOGMM-0.02 and SOGMM-0.03 show the effect of the bandwidth parameter σ . As expected from Fig. 3, the size of the model increases σ decreases. The σ parameter can be chosen based on the available computation as opposed to making an *a priori* guess about the complexity of the environments being modeled.

V. CONCLUSION

Computational modeling methods for multi-modal point cloud data lack the adaptability necessary for generalization across diverse scenes. This letter detailed a continuous probabilistic modeling approach that enables adaptation by estimating the number of components using self-organizing principles from information-theoretic learning. The quantitative and

qualitative results for the proposed method demonstrate its efficacy on diverse real-world scenes. Future work includes: (1) incremental mapping for streaming sensor data, (2) online and anytime selection of σ based on the available compute, (3) a highly parallelized implementation of the SOGMM system on an embedded GPU, and (4) enabling cross-modal inference.

REFERENCES

- [1] “Robotic 3D Scan Repository.” [Online]. Available: <http://kos.informatik.uni-osnabrueck.de/3Dscans/>
- [2] B. Ummerhofer, L. Prantl, N. Thuerey, and V. Koltun, “Lagrangian fluid simulation with continuous convolutions,” in *International Conference on Learning Representations*, 2020.
- [3] K.-A. Aliev, A. Sevastopolsky, M. Kolos, D. Ulyanov, and V. Lempitsky, “Neural Point-Based Graphics,” in *Computer Vision – ECCV 2020*, A. Vedaldi, H. Bischof, T. Brox, and J.-M. Frahm, Eds. Cham: Springer International Publishing, 2020, vol. 12367, pp. 696–712.

- [4] W. Tabib, K. Goel, J. Yao, C. Boirum, and N. Michael, "Autonomous Cave Surveying With an Aerial Robot," *IEEE Trans. Robotics*, pp. 1–17, 2021.
- [5] B. Eckart, "Compact Generative Models of Point Cloud Data for 3D Perception," Ph.D. dissertation, Carnegie Mellon University, Pittsburgh, PA, USA, Oct. 2017.
- [6] B. Eckart, K. Kim, A. Troccoli, A. Kelly, and J. Kautz, "Accelerated Generative Models for 3D Point Cloud Data," in *2016 IEEE Conference on Computer Vision and Pattern Recognition (CVPR)*. Las Vegas, NV, USA: IEEE, Jun. 2016, pp. 5497–5505.
- [7] S. Srivastava and N. Michael, "Efficient, Multifidelity Perceptual Representations via Hierarchical Gaussian Mixture Models," *IEEE Trans. Robotics*, vol. 35, no. 1, pp. 248–260, Feb. 2019.
- [8] C. O'Meadhra, W. Tabib, and N. Michael, "Variable Resolution Occupancy Mapping Using Gaussian Mixture Models," *IEEE Robot. Autom. Letters*, vol. 4, no. 2, pp. 2015–2022, Apr. 2019.
- [9] K. Goel, W. Tabib, and N. Michael, "Rapid and High-Fidelity Subsurface Exploration with Multiple Aerial Robots," in *Proc. of the Intl. Sym. on Exp. Robot.*, 2021, pp. 436–448.
- [10] M. Corah, C. O'Meadhra, K. Goel, and N. Michael, "Communication-Efficient Planning and Mapping for Multi-Robot Exploration in Large Environments," *IEEE Robot. Autom. Letters*, vol. 4, no. 2, pp. 1715–1721, Apr. 2019.
- [11] W. Tabib, C. O'Meadhra, and N. Michael, "On-manifold gmm registration," *IEEE Robot. Autom. Letters*, vol. 3, no. 4, pp. 3805–3812, 2018.
- [12] A. Dhawale and N. Michael, "Efficient Parametric Multi-Fidelity Surface Mapping," in *Robotics: Science and Systems XVI*. Proc. of Robot.: Sci. and Syst., Jul. 2020.
- [13] G. J. McLachlan and S. Rathnayake, "On the number of components in a Gaussian mixture model: Number of components in a Gaussian mixture model," *Wiley Interdisciplinary Reviews: Data Mining and Knowledge Discovery*, vol. 4, no. 5, pp. 341–355, Sep. 2014.
- [14] H. Akaike, "A new look at the statistical model identification," *IEEE Trans. on Automatic Control*, vol. 19, no. 6, pp. 716–723, Dec. 1974.
- [15] G. Schwarz, "Estimating the Dimension of a Model," *The Annals of Statistics*, vol. 6, no. 2, pp. 461–464, 1978.
- [16] M. H. Hansen and B. Yu, "Model Selection and the Principle of Minimum Description Length," *Journal of the American Statistical Association*, vol. 96, no. 454, pp. 746–774, Jun. 2001.
- [17] H. Attias, "A Variational Bayesian Framework for Graphical Models," in *Advances in Neural Information Processing Systems*, vol. 12. MIT Press, 1999.
- [18] D. M. Blei and M. I. Jordan, "Variational inference for Dirichlet process mixtures," *Bayesian Analysis*, vol. 1, no. 1, pp. 121–143, Mar. 2006.
- [19] A. Elfes, "Using occupancy grids for mobile robot perception and navigation," *Computer*, vol. 22, no. 6, pp. 46–57, Jun. 1989.
- [20] W. Tabib, R. Whittaker, and N. Michael, "Efficient multi-sensor exploration using dependent observations and conditional mutual information," in *IEEE Intl. Sym. on Safety, Security, and Rescue Robotics*, Oct. 2016, pp. 42–47.
- [21] M. Magnusson, A. Lilienthal, and T. Duckett, "Scan registration for autonomous mining vehicles using 3D-NDT," *Journal of Field Robotics*, vol. 24, no. 10, pp. 803–827, 2007.
- [22] H. Oleynikova, Z. Taylor, M. Fehr, R. Siegart, and J. Nieto, "Voxblox: Incremental 3D Euclidean Signed Distance Fields for on-board MAV planning," in *Proc. of the IEEE/RSJ Intl. Conf. on Intell. Robots and Syst.*, Sep. 2017, pp. 1366–1373.
- [23] A. Hornung, K. M. Wurm, M. Bennewitz, C. Stachniss, and W. Burgard, "OctoMap: An efficient probabilistic 3D mapping framework based on octrees," *Auton. Robots*, vol. 34, no. 3, pp. 189–206, Apr. 2013.
- [24] D. Duberg and P. Jensfelt, "UFOMap: An Efficient Probabilistic 3D Mapping Framework That Embraces the Unknown," *IEEE Robot. Autom. Letters*, vol. 5, no. 4, pp. 6411–6418, Oct. 2020.
- [25] N. Funk, J. Tarrío, S. Papatheodorou, M. Popović, P. F. Alcantarilla, and S. Leutenegger, "Multi-Resolution 3D Mapping With Explicit Free Space Representation for Fast and Accurate Mobile Robot Motion Planning," *IEEE Robot. Autom. Letters*, vol. 6, no. 2, pp. 3553–3560, Apr. 2021.
- [26] S. T. O'Callaghan and F. T. Ramos, "Gaussian process occupancy maps," *J. Intl. & Robot. Research*, vol. 31, no. 1, pp. 42–62, Jan. 2012.
- [27] F. Ramos and L. Ott, "Hilbert maps: Scalable continuous occupancy mapping with stochastic gradient descent," *J. Intl. & Robot. Research*, vol. 35, no. 14, pp. 1717–1730, Dec. 2016.
- [28] E. Zobeidi, A. Koppel, and N. Atanasov, "Dense Incremental Metric-Semantic Mapping for Multiagent Systems via Sparse Gaussian Process Regression," *IEEE Trans. Robotics*, pp. 1–21, 2022.
- [29] Z. Yan, X. Wang, and H. Zha, "Online Learning of a Probabilistic and Adaptive Scene Representation," in *Proc. of the Intl. Conf. on Computer Vision*, Jun. 2021, pp. 13 106–13 116.
- [30] B. Mildenhall, P. P. Srinivasan, M. Tancik, J. T. Barron, R. Ramamoorthi, and R. Ng, "NeRF: Representing Scenes as Neural Radiance Fields for View Synthesis," in *Computer Vision – ECCV, 2020*, pp. 405–421.
- [31] J. Navarrete, D. Viejo, and M. Cazorla, "Compression and registration of 3D point clouds using GMMs," *Pattern Recognition Letters*, vol. 110, pp. 8–15, Jul. 2018.
- [32] H. Dong, J. Yu, Y. Xu, Z. Xu, Z. Shen, J. Tang, Y. Shen, and Y. Wang, "MR-GMMapping: Communication Efficient Multi-Robot Mapping System via Gaussian Mixture Model," *IEEE Robot. Autom. Letters*, vol. 7, no. 2, pp. 3294–3301, Apr. 2022.
- [33] N. Greggio, A. Bernardino, C. Laschi, P. Dario, and J. Santos-Victor, "Fast estimation of Gaussian mixture models for image segmentation," *Machine Vision and Applications*, vol. 23, no. 4, pp. 773–789, Jul. 2012.
- [34] D. Arthur and S. Vassilvitskii, "K-means++: The advantages of careful seeding," in *Proceedings of the Eighteenth Annual ACM-SIAM Symposium on Discrete Algorithms*, ser. SODA '07. USA: Society for Industrial and Applied Mathematics, Jan. 2007, pp. 1027–1035.
- [35] S. Srivastava, "Efficient, multi-fidelity perceptual representations via hierarchical gaussian mixture models," Master's thesis, Carnegie Mellon University, Pittsburgh PA, August 2017.
- [36] W. Tabib, K. Goel, J. Yao, M. Dabhi, C. Boirum, and N. Michael, "Real-Time Information-Theoretic Exploration with Gaussian Mixture Model Maps," in *Proc. of Robot.: Sci. and Syst.* Robotics: Science and Systems Foundation, Jun. 2019.
- [37] J. A. Bilmes *et al.*, "A gentle tutorial of the em algorithm and its application to parameter estimation for gaussian mixture and hidden markov models," *Intl. computer science institute*, vol. 4, no. 510, p. 126, 1998.
- [38] H. G. Sung, "Gaussian Mixture Regression and Classification," Ph.D. dissertation, Rice University, Houston, Texas, May 2004.
- [39] J. C. Principe, *Information Theoretic Learning: Renyi's Entropy and Kernel Perspectives*, ser. Information Science and Statistics. New York: Springer, 2010.
- [40] S. Rao, A. d. M. Martins, and J. C. Principe, "Mean shift: An information theoretic perspective," *Pattern Recognition Letters*, vol. 30, no. 3, pp. 222–230, Feb. 2009.
- [41] Y. Cheng, "Mean shift, mode seeking, and clustering," *IEEE Transactions on Pattern Analysis and Machine Intelligence*, vol. 17, no. 8, pp. 790–799, Aug. 1995.
- [42] D. Comaniciu and P. Meer, "Mean shift: A robust approach toward feature space analysis," *IEEE Transactions on Pattern Analysis and Machine Intelligence*, vol. 24, no. 5, pp. 603–619, May 2002.
- [43] M. Á. Carreira-Perpiñán, "Fast nonparametric clustering with Gaussian blurring mean-shift," in *Proceedings of the 23rd International Conference on Machine Learning - ICML '06*. Pittsburgh, Pennsylvania: ACM Press, 2006, pp. 153–160.
- [44] J. Jang and H. Jiang, "MeanShift++: Extremely Fast Mode-Seeking With Applications to Segmentation and Object Tracking," in *Proc. of the Intl. Conf. on Computer Vision*. Nashville, TN, USA: IEEE, Jun. 2021, pp. 4100–4111.
- [45] Q.-Y. Zhou and V. Koltun, "Dense scene reconstruction with points of interest," *ACM Trans. on Graphics*, vol. 32, no. 4, pp. 1–8, Jul. 2013.
- [46] J. Wang and B. Englot, "Fast, accurate gaussian process occupancy maps via test-data octrees and nested bayesian fusion," in *Proc. of the IEEE Intl. Conf. on Robot. and Autom.* IEEE, 2016, pp. 1003–1010.